Physicochem. Probl. Miner. Process., 59(2), 2023, 163418

http://www.journalssystem.com/ppmp

Physicochemical Problems of Mineral Processing

ISSN 1643-1049

© Wroclaw University of Science and Technology

Substitution mechanism of rare earths at fluorapatite characteristic sites: experimental and computational calculations

Jun Xie

State Key Laboratory of Mining Response and Disaster Prevention and Control in Deep Coal Mines, Anhui University of Science and Technology, Huainan 232001, China

Department of Materials Science and Engineering, Anhui University of Science and Technology, Huainan 232001, China

Corresponding author: jxie@aust.edu.cn

Abstract: Rare earths (REs) containing phosphate rock is a potential REs resource. The unclear occurrence mechanism of REs in phosphorite limits its further development and utilization. Fluorapatite (FAP) is the main REs-bearing target mineral in phosphorite, the microscopic mechanism of REs entering FAP still needs to be further studied from the electronic scale. In this paper, the doping mechanism of REs in FAP was studied by experiment combined with GGA+U calculation. The XRD, SEM, and FT-IR characterization results of hydrothermal synthesis products showed that REs (La, Ce, Nd, and Y) entered FAP crystal, and one of every 20 Ca atoms was replaced by a REs atom. The GGA+U calculation indicated that La-O/F, Ce-O/F, Nd-O/F, and Y-O/F were ionic bonds in general, and the bonding strength of La-O/F, Ce-O/F, Nd-O/F, and Y-O/F increased gradually with atomic number. The substitution difference of La, Ce, Nd, and Y was mainly caused by the gain and loss of electrons in f and d orbitals. The substitution mechanism of REs at the characteristic sites of Fap was studied, which provided a theoretical reference for the selective recovery of REs from phosphorus blocks.

Keywords: rare earth, phosphorite, doping, electronic properties, computational calculations

1. Introduction

Rare earths (REs) mainly existed in three mineral forms in nature, including adsorption on clay minerals by hydrated or hydroxyl hydrate cation, occurrence in the mineral lattice as ionic compounds, and occurrence in minerals as impurity elements in isomorphism(Dushyantha et al., 2020). The first two forms of ores had a high RE content and were easy to extract and recover. Due to large-scale industrial consumption, traditional RE-rich ores had been developed and utilized in large quantities, and RE resources were in short supply. It was urgent to find a RE reserve resource to meet the needs of industrial production (Batapola et al., 2020; Ji and Zhang, 2021). Phosphate contained all Lanthanides except Pm, in which the content of ΣRE (the total RE) was 1098~1688 ppm(Xiqiang et al., 2020). From this perspective, phosphate was a reserved RE resource and had great development value. The four REs (La, Ce, Nd, and Y) were especially enriched among all REs in phosphorite and mainly occurred in the target mineral fluorapatite (FAP) (Zhang et al., 2021). Therefore, the recovery of REs from phosphorus blocks often required preconcentration of FAP. However, the cost-effective recovery of FAP from phosphorus blocks remained a challenge. The deep reason for REs substitution in FAP lattice was not clear, especially from the electronic scale.

It was a consensus that RE was isomorphic in FAP (Chen et al., 2013). The reason why RE entered FAP may be attributed to the fact that the radius of RE ions (0.0848~0.106nm) was close to that of calcium ions (0.099nm) (Fleet and Pan, 1995a). However, there were two different Ca sites (Ca1 and Ca2) in FAP. Whether RE occupied Ca1 or Ca2 sites and the occupation number of RE in corresponding sites still needed to be further studied.

The research on the structural occupation of RE in FAP speculated that most of the REs in phosphorite belong to Light REs, such as La, Ce, Nd, Sm, etc., which mainly occupied the smaller Ca2

DOI: 10.37190/ppmp/163418

position (Fleet and Pan, 1995b, 1995a, 1997). With the increase of atomic number, the Heavy REs were easier to occupy in the Ca1 position, so the occupation ratio of different RE ions in Ca1 and Ca2 positions gradually decreased, such as the occupying ratios of La, Ce, Pr, Nd in Ca2 to Ca1 were 4.04, 3.67, 3.30 and 2.92 respectively (Fleet et al., 2000; Fleet and Pan, 1994, 1995b, 1995a, 1997; Hughes et al., 1991; Pan et al., 2002; Pan and Fleet, 2002). The above research results were mainly based on X-ray diffraction. The bonding law of REs-O/F in electronic scale and the spatial regulation mechanism of RE atom at Ca site from the perspective of spatial coordination polyhedron were rarely involved.

Substitution energy or formation energy can measure the substitution ability of REs at the Ca site of FAP (Emery and Wolverton, 2017). Theoretically, the substitution energy was negative and REs can be substituted in FAP, and the substitution ability increased with the increase of the absolute value of substitution energy (Milojkov et al., 2020). Based on the first principle of Density Functional Theory (DFT), our research group calculated the substitution energies of La, Ce, Nd, and Y at the Ca site of FAP, which were -3.198 eV, -1.8982 eV, -3.443 eV, and 1.070 eV respectively (Wang et al., 2019). However, RE-doped FAP was a strong correlation system, and there was a strong Coulomb interaction between the electrons in the d and f orbitals of RE atoms (Xue et al., 2017). Only the GGA-PW91 correlation function was used in the above DFT calculation, and the description of the Coulomb interaction between the d and f orbitals of RE atoms may be inaccurate (Perdew et al., 1992). In addition, the above calculation only obtained the substitution energy of La, Ce, Nd, and Y at the FAP Ca site, which cannot completely show the substitution law of RE atoms at the Ca site. And the paper did not analyse the electronic distribution of RE substituted at the Ca site. DFT+U methods considered the Coulomb repulsion between local electrons with an opposite spin on the same atom, which can better describe the Coulomb interaction on atomic d and f orbits and were widely used in the calculation of related properties of magnetic systems and RE atoms (Anisimov et al., 1991; Himmetoglu et al., 2014; Jain et al., 2011). Therefore, in view of the above situation, based on the DFT+U method, we calculated the substitution energy of 15 rare earths and Y at the Ca site of FAP, and improved the calculation method, so that the description of the self-interaction of d and f orbits of REs was more reasonable, and the substitution energy calculation results were more accurate.

In this paper, FAP and La, Ce, Nd, and Y doped FAP were synthesized by the hydrothermal method. The diffraction characteristic peaks, infrared characteristic groups, crystal morphology, particle size and surface elements of the synthesized products were characterized by XRD, FT-IR and SEM-EDS. The possibility of La, Ce, Nd and Y entering the FAP lattice were determined from an experimental perspective. Based on the experiments, the doping characteristics of the REs at the Ca sites of FAP were studied by GGA+U calculations. The substitution energies of all RE atoms at Ca1 and Ca2 sites of FAP were calculated, and the substitution capacities of different RE atoms at Ca sites were compared. Then La, Ce, Nd, and Y were selected, and the Mulliken population of the corresponding RE-O/F were analysed. Finally, combined with the charge and differential charge distribution in RE doped supercells, the law of RE substitution at the Ca1 and Ca2 sites of FAP was clarified from the electronic scale. The relevant research provides a theoretical reference for the subsequent efficient recovery of REs from phosphorite.

2. Materials and methods

2.1. Synthesis of FAP and RE-doped FAP

There were a variety of natural FAP, most of which were found in igneous rocks, sedimentary rocks and metamorphic rocks, often closely symbiotic with minerals such as dolomite, calcite and quartz (Abouzeid et al., 2009). It was extremely difficult to obtain pure FAP by using various physical and chemical methods (including gravity, magnetic separation, flotation and chemical beneficiation methods, etc.) (Filippov et al., 2021; Huang et al., 2021). Fap containing impurities affected the doping process of REs, and it was difficult to control the selective entry of REs into the FAP lattice. Based on the above considerations, we choose synthetic FAP for the doping of REs, which can accurately control the doping process. FAP and RE-doped FAP were synthesized by the hydrothermal method. The $Ca(NO_3)_2$ or $CaCl_2$ was used as Ca source, Na_2HPO_4 or $(NH_4)_2HPO_4$ as P source, NaF or NH_4F as F source, oleic acid, octadecyl amine, disodium EDTA, CTAB, or acetyl dimethylamine as a surfactant, $RE(NO_3)_3$ as RE source, hydrochloric acid, nitric acid, and sodium hydroxide as pH regulator. The synthesis reactor was a laboratory small hydrothermal reactor and the specific synthesis steps were as follows: adding $Ca(NO_3)_2$, Na_2HPO_4, and NaF with the molar ratio of 5:3:1 into 300 ml tetrafluoroethylene lining, mixing evenly through magnetic stirring, adding a certain amount of EDTA disodium, CTAB, and other surfactants, adjusting the pH value, reacting at 180 ℃ and 3 Mpa for 12 h, cooling to room temperature to obtain FAP, according to a certain molar ratio of Ca/RE, RE-doped FAP was prepared by adding $RE(NO_3)_3$, reacting at 180 ℃, 3 Mpa for 12 h and cooling to room temperature. The product was washed and centrifuged with ethanol 3 times, and then washed and centrifuged with deionized water 3 times. The supernatant was poured out and dried in a 100 ℃ blast drying oven for 24 h to obtain RE-doped FAP crystal powder. By comparing the Ca element content and the total RE content in the natural FAP, we determined that the (Ca+RE)/RE ratio is 20:1, which was more consistent with the RE substitution situation in natural FAP. Therefore，in the experiment of doping RE in FAP, the molar ratio of Ca/RE was 20:1. The synthesis process is shown in Fig. 1.

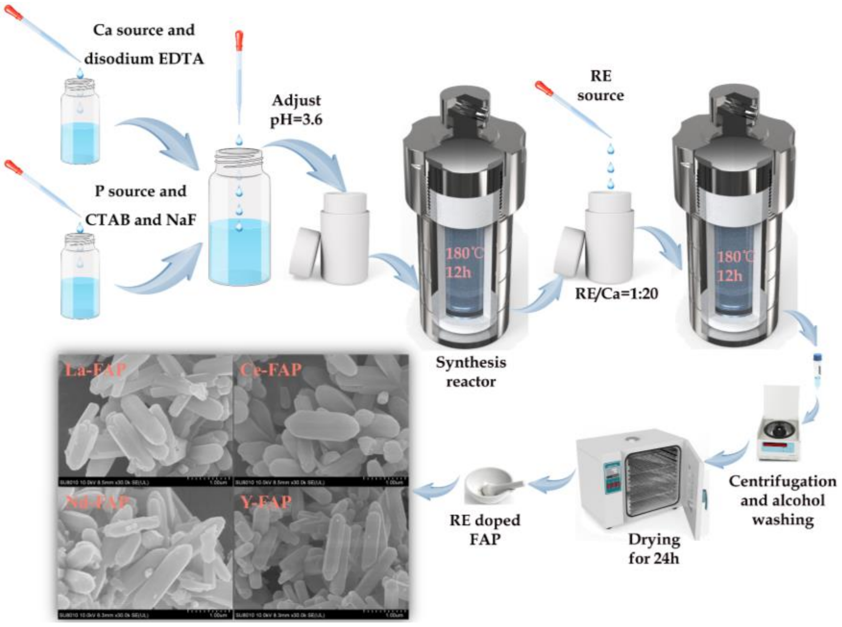

Fig. 1. Synthesis flow chart of FAP and RE-doped FAP

2.2. Characterization methods of synthetic products

2.2.1. XRD analysis

Continuous XRD was used to determine the mineral composition of phosphorite and La, Ce, Nd, Y doped FAP. Characteristic peaks of corresponding minerals were marked and semi-quantitative results of mineral composition were obtained. Test steps were as follows: ground the synthetic sample powder in agate mortar slightly and slowly, until the particle size of the product was less than 325 mesh (0.045 mm), accounting for 100%, and put it into a 100 ℃ blast drying oven for 2 h, take out 1-2 g dried sample in the groove of the sample rack (the test rack was cleaned and dried with ethanol in advance), and scrape the powder surface to be consistent with the frame surface. The test conditions were as follows: copper target was selected for the X-ray tube, the wavelength is 0.15406 nm, scattering slit (DS) was 1.0 mm, anti-scattering slit (SS) was 1.0 mm, receiving slit (RS) was 0.3 mm, tube voltage was 40 kV, tube current was 40 Ma, scanning range (2θ) was 5~110°, the step size was 0.01313°, each step was scanned for 15 s.

2.2.2. FT-IR analysis

FAP, RE-doped FAP, and potassium bromide powder were put into a 150 ℃ blast drying oven for 2 h. Then, the samples were fully ground, mixed, and pressed with an appropriate amount of potassium bromide. The resolution was 4 cm^{-1}, the scanning times were 16, and the scanning range was 400~4000 cm^{-1}. The representative characteristic peaks in the range of 400-1200 cm^{-1} were selected to analyze the characteristics of the synthesized products.

2.2.3. SEM-EDS analysis

SEM was used to analyze the morphology of the synthesized products, and the corresponding chemical elements were analyzed by EDS. SEM-EDS operation steps: firstly, put the sample into 150 ℃ blast drying oven for 2 h, took an appropriate amount of dry sample on the conductive adhesive, sprayed gold, put it into the sample chamber for vacuum, under the conditions of accelerating voltage of 30 kV, sputtering current of 40 Ma, got the crystal morphology of the sample, selected the characteristic area, got the element composition and semi-quantitative results of the sample, judged the accuracy of the synthesis.

2.3. Quantum chemistry calculation of FAP and RE-doped FAP

Firstly, an ideal FAP crystal structure was constructed. Then, RE-doped FAP was constructed. The representative FAP crystal structure was constructed according to the American Mineral Crystal Structure Database, as shown in Fig. 2. The order of the atomic stacking layer in the crystal cell from top to bottom was $Ca \rightarrow Ca_3(PO_4)_3F \rightarrow Ca\text{-}Ca \rightarrow Ca_3(PO_4)_3F \rightarrow Ca$(Xie et al., 2018). Two groups of Ca1 atoms (two in each group) form an atomic column perpendicular to the (001) crystal plane and two groups of Ca2 atoms (three in each group) form a terminal perpendicular to the c-axis, as shown in Fig. 2a. There are three terminals in the (001) crystal plane, namely (PO_4)-terminal, Ca-Ca-terminal, and Ca-terminal, corresponding to the purple, green and pink terminals(Xie et al., 2019). The FAP lattice constant ($a = b = 9.375$ Å, $c = 6.887$ Å, $a = \beta = 90°$, $\gamma = 120°$, space group $C26h\text{-}P6_3/m$) (Comodi et al., 2001) is shown in Fig. 2a and Fig. 2b.

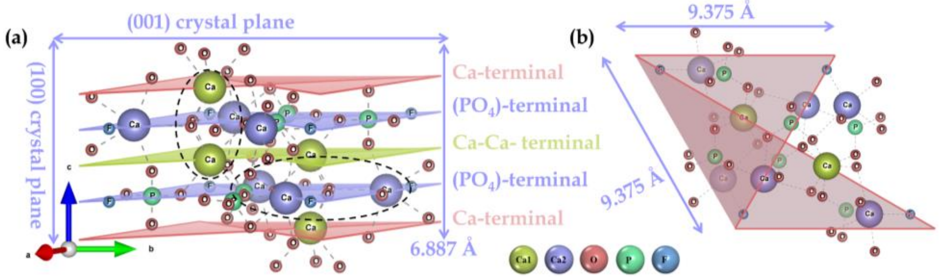

Fig. 2. Crystal structure of FAP, (a) side view; (b) top view

After constructing the FAP cell model, geometric optimization was carried out. All calculations were based on DFT and carried out by using the CASTEP module (Clark et al., 2005). Geometric optimization includes three aspects: Exchange-correlation function, Energy cut-off, and *K*-point in the Brillouin zone (Monkhorst and Pack, 1976). Broyden-Fletcher-Goldfarb-Shanno (BFGS) algorithm was used to optimize the bulk phase(Pfrommer et al., 1997). The interaction between valence electrons and ionic nuclei was described by ultra-soft pseudopotential (Vanderbilt, 1990). The geometric optimization was set according to the following convergence accuracy: the convergence accuracy of maximum force, maximum displacement and maximum stress were set to 0.05 eV/Å, 0.002 Å and 0.05 GPa, and the convergence accuracy of total energy and self-consistent iteration was set to 2.0×10^{-5} eV/atom and 1.0×10^{-6} eV/atom. All the atomic orbitals involved in the calculation are H $1S^1$, O $2s^22p^4$, F $2s^22p^5$, P $3s^23p^3$, Ca $3s^23p^64s^2$, La $5s^25p^65d^16s^2$, Ce $4f^15s^25p^65d^16s^2$, Nd $4f^45s^25p^66s^2$ and Y $4d^15s^2$ respectively. Considering the optimization results of the Exchange-correlation function, energy cut-off, and K-point in the Brillouin zone, the Exchange-correlation function GGA-PBE (Perdew et al., 1996), energy cut-off 540 eV, and K-point in Brillouin zone 3×3×4 were selected as the basic parameter of geometric optimization. The energy of the FAP single cell was the lowest and the corresponding structure was the most stable. The optimized FAP crystal structure was shown in Fig. 3, with lattice constant ($a = b = 9.377$ Å, $c = 6.884$ Å, $a = \beta = 90°$, $\gamma = 120°$, space group $C26h\text{-}P6_3/m$) and experimental values ($a = b = 9.375$ Å, $c = 6.887$ Å, $a = \beta = 90°$, $\gamma = 120°$, space group $C26h\text{-}P6_3/m$) agreed well, and the optimization errors of a, b and c were less than 0.05%.

Based on the geometry optimization, the 1×2×1 supercell was selected for studying the doping mechanism of RE in the Ca site. Ca1 and Ca2 atoms were replaced by RE (La, Ce, Nd, Y) in turn, and the RE-doped FAP models were constructed, including the following substitution types: single RE substituted Ca1 (Fig. 4a) and single RE substituted Ca2 (Fig. 4b). The corresponding coordination polyhedral structures were shown in Fig. 4c and Fig. 4d. The coordination polyhedron of RE atoms at Ca1 and Ca2 sites was shown by the arrow in Fig. 4c and Fig. 4d.

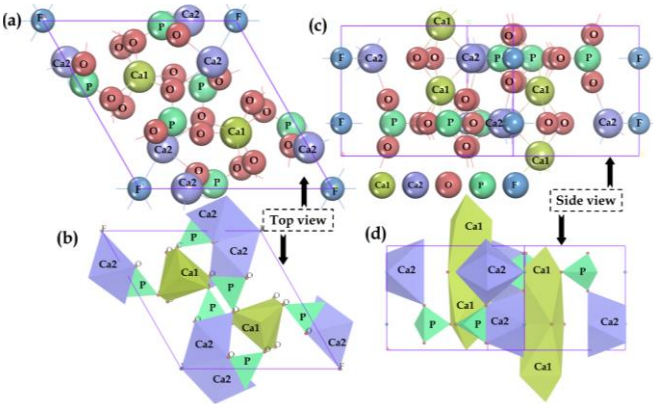

Fig. 3. FAP crystal structure after geometric optimization, (a-b) ball-and-stick model; (c-d) coordination polyhedron model

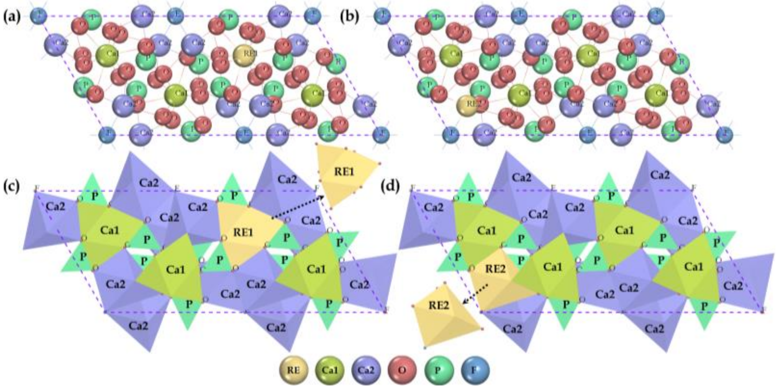

Fig. 4. Replacement model of RE in Ca site, (a) one RE replaces Ca1; (b) one RE replaces Ca2; (c) coordination polyhedron configuration of RE doped at Ca1 site; (d) coordination polyhedron configuration of RE doped at Ca2 site

Because RE-doped FAP was a strong correlation system, there was a strong Coulomb interaction between the electrons in the d and f orbitals of RE atoms. Since the generalized gradient approximation (GGA) and the local density approximation (LDA) alone cannot be used to accurately describe the d/f-state electrons and the localized p-state electrons of the oxygen element, the Hubbard parameter U (repulsion energy) was used to describe this strong correlation in the model, that was, the electronic structure of compounds containing RE atoms and localized oxygen atoms was described by GGA+U method. The spin polarization was also checked in the whole process of GGA+U calculation. The U_{La}=1 eV, U_{Ce}=6 eV, U_{Nd}=6 eV, and U_{Y}=2 eV were applied on La 5d, Ce 4f, Nd 4f, and Y 4d orbits respectively, the corresponding cell parameters were shown in Table 1.

Table 1. Effect of U value on structural parameters of RE doped FAP

U values (eV)	a=b (Å)	c (Å)
U_{La5d} = 1.0	9.451	6.991
experimental value(Liu et al., 2016)	9.431	6.926
U_{Ce4f} = 6.0	9.365	6.940
experimental value(Hughes et al., 1991)	9.391	6.899
U_{Nd4f} = 6.0	9.359	6.920
experimental value(Boyer et al., 1998)	9.394	6.901
U_{Y4d} = 2.0	9.399	6.920
experimental value(Rout and Agrawal,	9.830	7.350

3. Results and discussion

3.1. Characterization of synthetic products

3.1.1. Analysis of chemical phase and characteristic group

The chemical phase of the synthesized product was analysed by XRD. The XRD diffraction patterns and the FT-IR of synthesized FAP and La, Ce, Nd, Y-doped FAP were shown in Fig. 5a and Fig.5b. Fig. 5a showed that the corresponding characteristic peaks of FAP and La, Ce, Nd, and Y-doped FAP were in good agreement with the standard card (PDF-000042), few impurity peaks were occasionally found, which may be the characteristic peak of RE-bearing phosphate, and the corresponding content was very small, which had little effect on the overall performance of RE-doped FAP. The FT-IR of FAP and La, Ce, Nd, Y-doped FAP was shown in Fig. 5b. The characteristic peaks near 1100, 1070 and 1048 cm^{-1} were the peaks of $(PO_4)^{3-}$ ion in FAP v3 (asymmetric stretching vibration peak); the characteristic peaks near 607 and 570 cm^{-1} were the peak of $(PO_4)^{3-}$ ion in FAP v4 (in-plane bending vibration peak); the characteristic peak at 966 cm^{-1} was the peak of $(PO_4)^{3-}$ ion in FAP v1 (symmetric stretching vibration) (Wang et al., 2018). The fundamental frequency vibration of v1、v3、v4 of La, Ce, Nd, and Y doped FAP were consistent with that of FAP, and the main structure of RE-doped FAP was consistent with that of FAP. The difference lies in the slight shift of some characteristic peaks, which may be due to the small group difference caused by the substitution of RE elements at the Ca site of FAP. Through XRD phase qualitative and FT-IR group analysis, it was confirmed that the synthesized phases were FAP and RE-doped FAP, with few impurities occasionally, and the overall synthesis process was accurate.

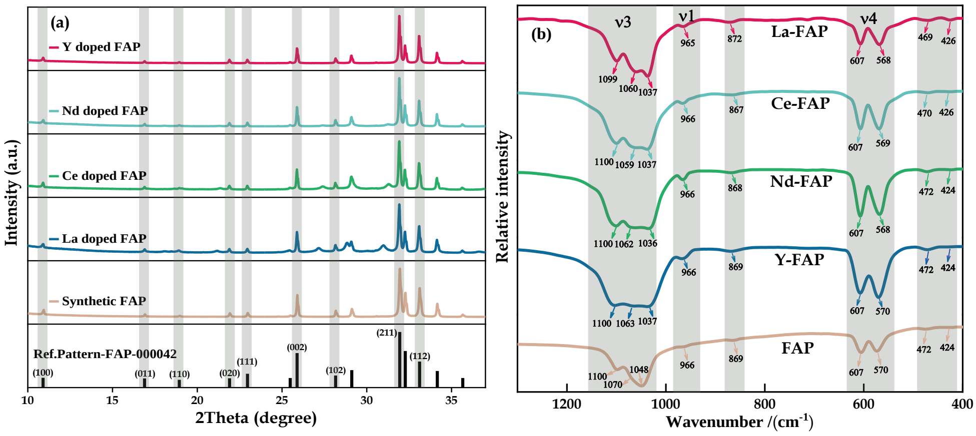

Fig. 5. XRD patterns (a) and FT-IR (b) of synthesized FAP and La, Ce, Nd, Y doped FAP

3.1.2 Crystal morphology and surface element analysis

SEM of FAP crystal powder with different magnifications was shown in Fig. 6a and Fig. 6c. The FAP had a complete crystal shape and was generally hexagonal columnar, which was consistent with the single-crystal shape of natural FAP. Fig. 6a and Fig. 6b showed that the length of synthesized FAP was from 0.24 μm to 1.46 μm. Among them, 0.4~0.6 μm accounted for 34.95%, 0.6~0.8 μm accounted for 30.10%, 0.8~1.0 μm accounted for 14.56%, and the proportion of other lengths was relatively small. Fig. 6c and Fig. 6d showed that FAP has high purity and the atomic ratio of O, F, P, and Ca was 74.34:6.10:19.21:31.02, which was close to the theoretical atomic ratio of 12:1:3:5. Fig. 6e and Fig. 6f showed that the crystal shape of La-doped FAP was generally like that of FAP, but La-doped FAP was longer and two ends gradually became sharp. The length of synthesized La-doped FAP was from 0.50 μm to 2.41 μm. Fig. 6g and Fig. 6h showed the atomic ratio of O, F, P, Ca, La was 56.40:4.68:14.30:23.71:1.20, and the atomic ratio of O, F, P, Ca was close to the theoretical atomic ratio of 12:1:3:5. The atomic ratio of (Ca+La)/La was about 20.76, about 1 Ca was replaced by La among 20 Ca atoms in the FAP cell. Fig. 6i and Fig. 6j showed that the crystal shape of Ce-doped FAP was like that of La-doped FAP. The average length of Ce-doped FAP was close to that of La-doped FAP. The length of synthesized Ce-doped FAP was from 0.60 μm to 2.18 μm. Fig. 6k and Fig. 6l showed that the atomic ratio of O, F, P, Ca, and Ce was 57.07:3.71:16.11:23.06:1.12, and the atomic ratio of (Ca+Ce)/Ce was about 21.59. About 1 Ca was replaced by Ce among 20 Ca atoms in the FAP cell. Fig. 6m and Fig. 6n showed that the crystal shape of Nd-doped FAP was like that of La and Ce doped FAP, the length of synthesized Nd-doped FAP was from 0.46 μm to 1.99 μm. Fig. 6o and Fig. 6p showed that the atomic ratio of O, F, P, Ca, and Nd was 55.85:4.66:14.20:24.19:1.25. The atomic ratio of (Ca+Nd)/Nd was about 20.35, about 1 Ca was replaced by Nd among 20 Ca atoms of the FAP cell. Fig. 6q and Fig. 6r showed that the crystal shape of Y-doped FAP was like La, Ce, and Nd-doped FAP, but the particle size distribution was more uniform and smaller than La, Ce, and Nd-doped FAP. The length of synthesized Y-doped FAP was from 0.42 μm to 1.79 μm. Fig. 6s and Fig. 6t showed that the atomic ratio of O, F, P, Ca, and Y was 55.90:4.65:14.19:23.65:1.24. The atomic ratio of (Ca+Y)/Y was about 20.07, and about 1 Ca was replaced by Y in 20 Ca atoms of the FAP cell.

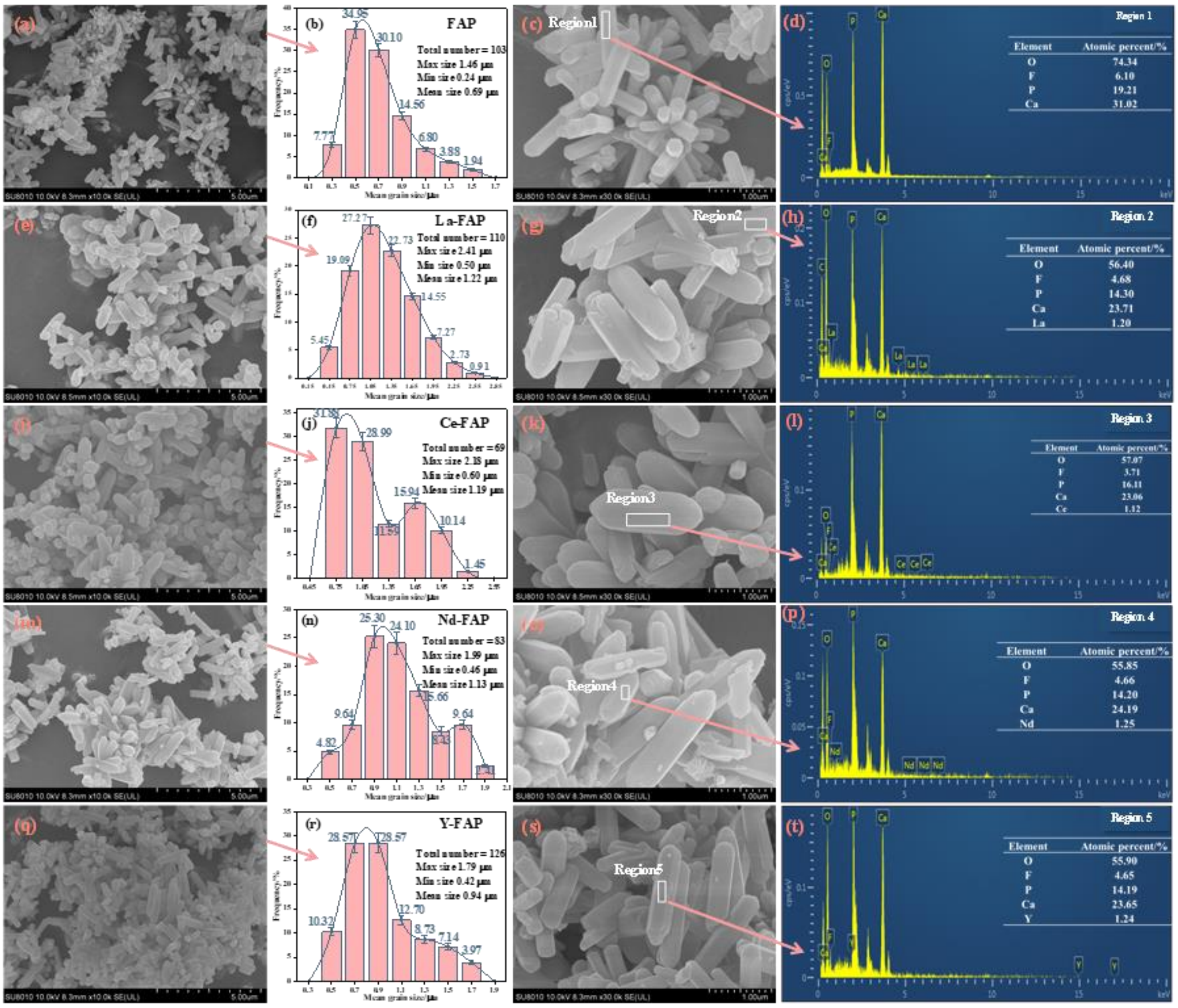

Region 1

Element	Atomic percent/%
O	74.34
F	6.10
P	19.21
Ca	31.02

Region 2

Element	Atomic percent/%
O	56.40
F	4.68
P	14.30
Ca	23.71
La	1.20

Region 3

Element	Atomic percent/%
O	57.07
F	3.71
P	16.11
Ca	23.06
Ce	1.12

Region 4

Element	Atomic percent/%
O	55.85
F	4.66
P	14.20
Ca	24.19
Nd	1.25

Region 5

Element	Atomic percent/%
O	55.90
F	4.65
P	14.19
Ca	23.65
Y	1.24

Fig. 6. SEM-EDS and particle size of synthetic FAP and La, Ce, Nd, Y-doped FAP

3.2. Electronic properties of FAP and RE-doped FAP

The substitution energy, bonding density of RE atoms, Mulliken charge population, Mulliken bond population, charge density, and differential charge density of RE doped at Ca1 and Ca2 sites of FAP were analysed.

3.2.1. Substitution energy analysis of RE at Ca site

There were Ca1 and Ca2 sites in FAP, and the chemical environment around the two Ca sites is quite different. RE can be substituted at both Ca1 and Ca2 sites, but the degree of substitution was different. The degree of substitution difficulty can be measured by substitution energy or formation energy. The substitution energies of 15 REs (La-Lu) and Y at Ca1 and Ca2 sites were calculated by DFT+U to clarify the difficulty of RE substitution from the perspective of energy. Substitution energy was defined as follows (Emery and Wolverton, 2017):

$$\Delta E=(E_{RE}^{Total}-E_{RE})-(E_{Bulk}^{Total}-E_{Ca}) \tag{1}$$

E_{RE}^{Total} and E_{Bulk}^{Total} represents the total energy of FAP with and without RE, respectively. E_{RE} and E_{Ca} represents the total energy of one RE atom and one Ca atom respectively. Theoretically, ΔE is a negative value, which means that the substitution process can occur, and the greater the absolute value of ΔE, the more likely the substitution reaction is to occur.

The substitution energy of 15 REs and Y at the Ca1 and Ca2 sites of FAP was shown in Fig. 7. The substitution energy of RE was generally "oblique W-shape" and had obvious "gadolinium (Gd) breaking phenomenon". There was a small difference in the substitution energies between Ca1 and Ca2 sites, and the overall trend was the same. The substitution energy of RE was generally negative at the Ca1 and Ca2 sites. Theoretically, RE can be substituted at the Ca1 (or Ca2) site. The substitution energy of Light Rare Earth (LRE) from La-Eu was negative and the absolute value increased gradually, indicating that the substitution ability of LRE at the Ca1 (or Ca2) site increased gradually with the increase of atomic number. Due to the contraction of lanthanide, the ion radius decreased gradually, and the radius was the main influencing factor. From Gd to Er, there was an obvious peak in the substitution of Heavy Rare Earth (HRE), which first changed from a negative value to a positive value, increased to the maximum at Dy, and then decreased from a positive value to a negative value. The substitution energy from Er to Lu was negative and the absolute value decreased gradually. Based on the above, the absolute value of LRE substitution energy at the Ca1 (or Ca2) site increased monotonically with the increase of atomic number. The substitution ability of LRE increased gradually and reached the maximum at Gd. The substitution law of HRE at the Ca1 (or Ca2) site did not show monotonic change, it was necessary to comprehensively consider the atomic coordination ability and spatial configuration for further analysis.

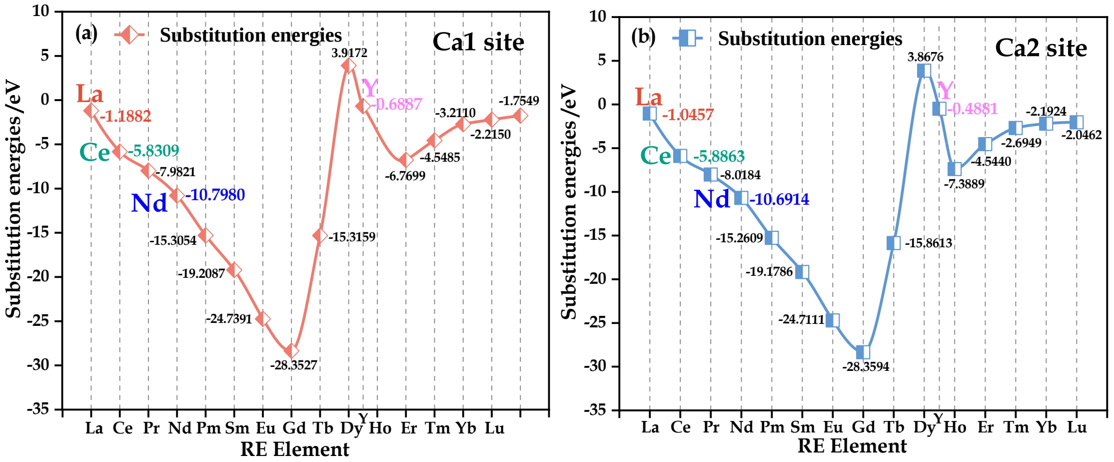

Fig. 7. Substitution energy of RE at Ca1 (a) and Ca2 (b) sites

3.2.3. Analysis of Mulliken population

Ca sites in FAP were the reaction active sites, and RE atoms can replace Ca atoms in the form of isomorphism (Jin et al., 2017). The bond strength of RE atoms at Ca site will change after substitution, and the change rule of RE-O or RE-F can be quantitatively determined by Mulliken population. Mulliken population included Mulliken charge population and Mulliken bond population. Mulliken charge population reflected the charge transfer of RE at the corresponding sites, and the Mulliken bond population reflected the bonding strength of RE at the corresponding sites.

Table 2 showed Mulliken charge populations of La, Ce, Nd, Y, and Ca at Ca1 site and gave quantitative results of electron transfer of different orbits. The orbits of Ca atom involved in the calculation is $3s^2 3p^6 4s^2$. The electrons in *4s* orbit of Ca excited and transferred to *3d* orbit. During bonding, some electrons transferred to other atoms and some stayed in *3d* orbit. Specifically, the *4s* orbit of Ca1 lost 2 electrons, the *3d* and *3s* orbits gained 0.56 and 0.13 electrons respectively, and a total of 1.31 electrons were lost. The valence shell of La, Ce, Nd, Y involved in the calculation were $5s^25p^65d^16s^2$, $4f^15s^25p^65d^16s^2$, $4f^45s^25p^66s^2$ and $4d^15s^2$. Among them, the 6s orbit of La lost 1.97 electrons, and the *5p* and *5d* orbits got 0.09 and 0.58 electrons, and overall, 1.30 electrons were lost. The 6s and 5d orbits of Ce lost 1.86 and 0.16 electrons, while the *4f* and *5p* orbits gained 0.84 and 0.07 electrons, respectively, eventually 1.15 electrons were lost. The 6s orbit of Nd lost 1.89 electrons, while the *4f* orbital, *5p* orbital and *5d* orbital gained 0.03 electrons, 0.02 electrons and 0.74 electrons, 1.10 electrons were lost in total. The *5s* orbit of Y lost 1.79 electrons, while the *4p* and the *4d* orbits gained 0.04 electrons and 0.70 electrons, respectively, and the Y atom overall lost 1.05 electrons. From Table 2, La, Ce, Nd, Y and Ca were all in a state of loss of electrons at the Ca1 site, the number of lost electrons was between 1.05 and 1.31, and the lost electrons were transferred to the adjacent O atom. Ca atoms and four RE atoms all exhibited electron loss in the outermost s orbital, and the corresponding electron-acquired orbits were *5d*, *4f*, *5d*, and *4d*, respectively. Table 3 showed that the electron gains and loss of La, Ce, Nd, Y and Ca2 at the Ca2 site were like that at the Ca1 site and the number of electron loss was from 1.07 to 1.36. The lost electrons were transferred to the adjacent O and F atoms. At the Ca2 site, the change in electrons of La, Ce, Nd, Y showed characteristics like those at the Ca1 site. Specifically, the outermost 6s orbit lost electrons, and the corresponding *5d*, *4f*, *5d* and *4d* orbits got electrons.

Table 2. Mulliken charge population of La, Ce, Nd, Y, Ca1 at Ca1 site

Atoms	Atomic orbital				Valence electron total	Number of electrons gained and lost (electrons)	Valence shell
	s	*p*	*d*	*f*			
La	2.03	6.09	1.58	0	9.70	lost 1.30	$5s^25p^65d^16s^2$
Ce	2.14	6.07	0.84	1.84	10.85	lost 1.15	$4f^15s^25p^65d^16$
Nd	2.11	6.02	0.74	4.03	12.90	lost 1.10	$4f^45s^25p^66s^2$
Y	0.21	0.04	1.70	0.00	1.95	lost 1.05	$4d^15s^2$
Ca1	2.13	6.00	0.56	0.00	8.69	lost 1.31	$3s^23p^64s^2$

Table 3. Mulliken charge population of La, Ce, Nd, Y, Ca2 at Ca2 site

Atoms	Atomic orbital				Valence electron total	Number of electrons gained and lost (electrons)	Valence shell
	s	*p*	*d*	*f*			
La	2.00	6.12	1.52	0	9.64	lost 1.36	$5s^25p^65d^16s^2$
Ce	2.15	6.09	0.83	1.75	10.82	lost 1.18	$4f^15s^25p^65d^16$
Nd	2.12	6.06	0.73	4.01	12.93	lost 1.07	$4f^45s^25p^66s^2$
Y	0.18	0.12	1.58	0.00	1.88	lost 1.12	$4d^15s^2$
Ca2	2.13	6.00	0.54	0.00	8.67	lost 1.33	$3s^23p^64s^2$

Mulliken bond populations were between 0 and 1, which reflected the ionic and covalent nature of the bond (Mulliken, 1955a). The larger the value, the stronger the bond covalence, the smaller the value, the stronger the bond ionic property (Mulliken, 1955b). Table 4 showed Mulliken populations of Ca1-O1/O2/O3, La-O1/O2/O3, Ce-O1/O2/O3, Nd-O1/O2/O3, and Y-O1/O2/O3 at Ca1 site, and showed bond types and gave quantitative results of bond strength. Similar results at Ca2 site of Ca2-O1/O2/O3/F, La-O1/O2/O3/F, Ce-O1/O2/O3/F, Nd-O1/O2/O3/F, and Y-O1/O2/O3/F were shown in Table 5. Mulliken bond population of Ca1-O1 (0.11), Ca1-O2 (0.09), and Ca1-O3 (0.03) decreased gradually, which corresponded to three groups of O atoms with different distances from Ca atoms, reflecting the non-uniformity of bonding between Ca and O. Mulliken bond population of La-O/F, Ce-O/F, Nd-O/F, Y-O/F at Ca1 and Ca2 sites was between 0.03 and 0.27, which contained both ionic bond and covalent bond components, however, there were great differences in bond strength. Mulliken population of La-O, Ce-O, Nd-O, Y-O showed an increasing trend at the Ca1 site. However, the difference between La-O, Ce-O, Nd-O, and Y-O was smaller than that of Ca1-O, indicating that substitution of La, Ce, Nd, Y at the Ca1 site leaded to the reduction of the bonding difference of RE-O1/O2/O3. The reason for this phenomenon was the spatial regulation of RE after substitution at the Ca1 site. Mulliken population of Ca2-F bond was the smallest (0.06) and the corresponding bonding strength was the lowest. The second smallest were Ca2-O2 and Ca2-F (0.11). Mulliken population of Ca2-O3 was the largest (0.14), and the corresponding bonding strength was the largest. When Ca2 was replaced by La, Ce, Nd, and Y, the overall bonding strength increased, but the bonding strength between RE-O1/O2/O3 and RE-F varied greatly. The results of Mulliken population, charge density and differential charge density obtained in our paper were compared with the results of previous literature (Wang et al., 2019). Both papers showed that after the replacement of rare earths at the Ca site, the covalency of RE-O and RE-F was enhanced compared with Ca-O and Ca-F, the difference was that the previous research only focused on the Ca2 site, while the Ca1 and Ca2 sites were analyzed in detail in our paper. In addition, the calculation based on the DFT+U method was more accurate for the self-interaction of the d and f orbitals of rare earth atoms, and the obtained Mulliken population, charge density and differential charge density data were more reliable. This result was also consistent with the literature research for structural analysis of calcium and lanthanum phosphosilicate apatites by Rietveld refinement (Fleet and Pan, 1997; Njema et al., 2013).

Many studies had shown that the atom Ca had some unsaturated bonds and played a key role on the common exposed surface of fluorapatite (Qiu et al., 2017; Xie et al., 2019). Since RE–O was more covalent than Ca–O and Ca-F, the RE atom with unsaturated bond exposed on the surface of RE-bearing fluorapatite will interact with oleic acid (a collector commonly used in FAP flotation) much more intensely compared to the FAP (Xie et al., 2018). Therefore, the higher the covalent value, the stronger the adsorption capacity of oleic acid on the mineral surface will be. From the above comprehensive analysis of the Mulliken population, the existence of REs substitution may be in favor of the fluorapatite flotation.

Table 4. Mulliken bond population and bond length of La-O, Ce-O, Nd-O, Y-O at Ca1 site

Atoms	Mulliken bond population			Bond length/Å		
	O1	O2	O3	O1	O2	O3
La	0.12	0.11	0.11	2.536	2.583	2.645
Ce	0.13	0.10	0.11	2.535	2.612	2.720
Nd	0.15	0.12	0.12	2.526	2.602	2.728
Y	0.22	0.18	0.17	2.483	2.556	2.575
Ca1	0.11	0.09	0.04	2.391	2.438	2.793

Table 5. Mulliken bond population and bond length of La-O/F, Ce-O/F, Nd-O/F, Y-O/F at Ca2 site

Atoms	Mulliken bond population				Bond length/Å			
	O1	O2	O3	F	O1	O2	O3	F
La	0.03	0.19	0.17	0.09	2.831	2.516	2.504	2.556
Ce	0.04	0.18	0.16	0.14	2.850	2.525	2.517	2.431
Nd	0.06	0.19	0.18	0.16	2.778	2.498	2.520	2.448
Y	0.04	0.27	0.27	0.21	2.638	2.468	2.444	2.420
Ca2	0.06	0.11	0.14	0.11	2.687	2.366	2.338	2.282

3.2.3. Analysis of charge density and differential charge density

Charge density directly showed the charge distribution range, and differential charge density directly showed the bonding situation. Combined with the Mulliken population, it was conducive to further analyzing the atomic bonding in space. The charge density and differential charge density at the Ca1 and Ca2 sites of FAP were shown in Fig. 8, as indicated by the black arrow. The Fig. 8a ~ Fig. 8d were the charge density isopotential, the cross section of charge density isopotential, differential charge density isopotential and the cross sections of differential charge density isopotential at Ca1 site respectively. The Fig. 8e ~ Fig. 8h were the charge density isopotential, the cross sections of charge density isopotential, differential charge density isopotential and the cross sections of differential charge density isopotential at Ca2 site respectively. The value of the charge density isopotential surface in Fig. 8a and Fig. 8e was 1eV, and the charges around Ca1 and Ca2 were globally distributed, and the closer to the center, the higher the charge density. The cross sections of the corresponding isopotential in Fig. 8b and Fig. 8f showed this rule visually, and it was obvious that the charge density at Ca1 site was higher than that at Ca2 site. In Fig. 8c and Fig. 8g, the value of isopotential surface of the differential charge density was 0.1eV, and the contour of the isopotential surface clearly showed the gain and loss of electrons of each atom, among them, the O atom had obtaining electrons characteristic, and the surrounding differential charge density was positive and green. Ca and P atoms loss of electrons obviously, and the surrounding differential charge was negative and yellow. The cross sections of the differential charge density isopotential surface in Fig. 8d and Fig. 8h clearly showed the bonding types between atoms. It was obvious that O *2s* and Ca *3p* orbits form *σ* bonding, and O *2p* and Ca *3p* orbits form *π* bonding. A strong covalent bond was formed between P and O and the sp^3 hybrid form of -PO_4- was obvious in the differential charge density diagram. The overall shape presented a tetrahedron and there were four strong σ bonds.

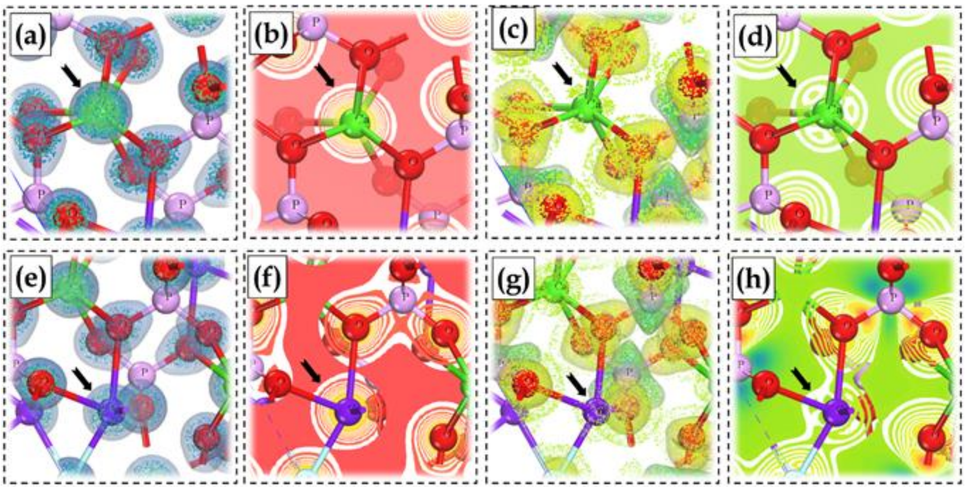

Fig. 8. Charge density and differential charge density of FAP at the Ca1(a-d) and Ca2 (e-h) sites. (a) charge density of isopotential (Ca1), (b) the cross sections of charge density isopotential (Ca1), (c) differential charge density isopotential (Ca1), (d) the cross sections of differential charge density isopotential (Ca1), (e) charge density isopotential (Ca2), (f) the cross sections of charge density isopotential (Ca2), (g) differential charge density isopotential (Ca2), (h) the cross sections of differential charge density isopotential surface (Ca2)

The charge density isopotential of La, Ce, Nd, and Y at Ca1 sites were shown in Fig. 9a ~ Fig. 9d, and the corresponding cross sections were shown in Fig. 9e ~ Fig. 9h. The differential charge density isopotential of La, Ce, Nd, and Y at Ca1 sites were shown in Fig. 9i ~ Fig. 9l, and the corresponding cross sections were shown in Fig. 9m ~ Fig. 9p. Fig. 9a ~ Fig. 9d showed that the isopotential surface of the extranuclear electrons of La, Ce, Nd and Y was 1eV, and the electrons in the equipotential surface were sporadically distributed and generally spherical. The distribution density of the extranuclear electrons of Ce and Nd was higher than that of La, and the distribution density of the extranuclear electrons of Y was the lowest. The cross section of the electron distribution of La, Ce and Nd in Fig. 9e ~ Fig. 9h showed that the extranuclear electrons were concentric rings, while the extranuclear electrons of Y splited into petals with the Y atom as the center. The closer the extra nuclear electrons of La, Ce, Nd and Y were to the center, the higher the corresponding density. Fig. 9e ~ Fig. 9h showed that the differential charge density of La1-O was like that of Ca1-O, which was an ionic bond. In addition to forming ionic bonds, Ce-O and Nd-O also formed covalent bonds to a certain extent, and the covalent bond formed by Nd1-O was stronger than that of Ce1-O. Mulliken bond populations of Ce1-O and Nd1-O were consistent with their differential charge density results. The differential charge density of Y1-O was like that of Ca1-O and La1-O, and generally showed an ionic bond, but the bond strength of Y1-O was greater than that of La1-O, Ce1-O, and Nd1-O. The possible reason was that the atomic numbers of Y and Ca1 were close. After Y replaces Ca1, there was a certain spatial adjustment, which will be further discussed in the influence of coordination polyhedron spatial configuration on the substitution of RE atoms.

The charge density isopotential of La, Ce, Nd, and Y at Ca2 site were shown in Fig. 10a ~ Fig. 10d, and the corresponding cross sections were shown in Fig. 10e ~ Fig. 10h. The differential charge density isopotential of La, Ce, Nd, and Y at Ca1 sites were shown in Fig. 10i ~ Fig. 10l, and the corresponding cross sections were shown in Fig. 10m ~ Fig. 10p. The charge density and differential charge density of Ca2 site showed the same change law as the Ca1. Compared with the Ca1 site, the differential charge density was greater and the corresponding bonding strength is greater, as shown in Fig. 10.

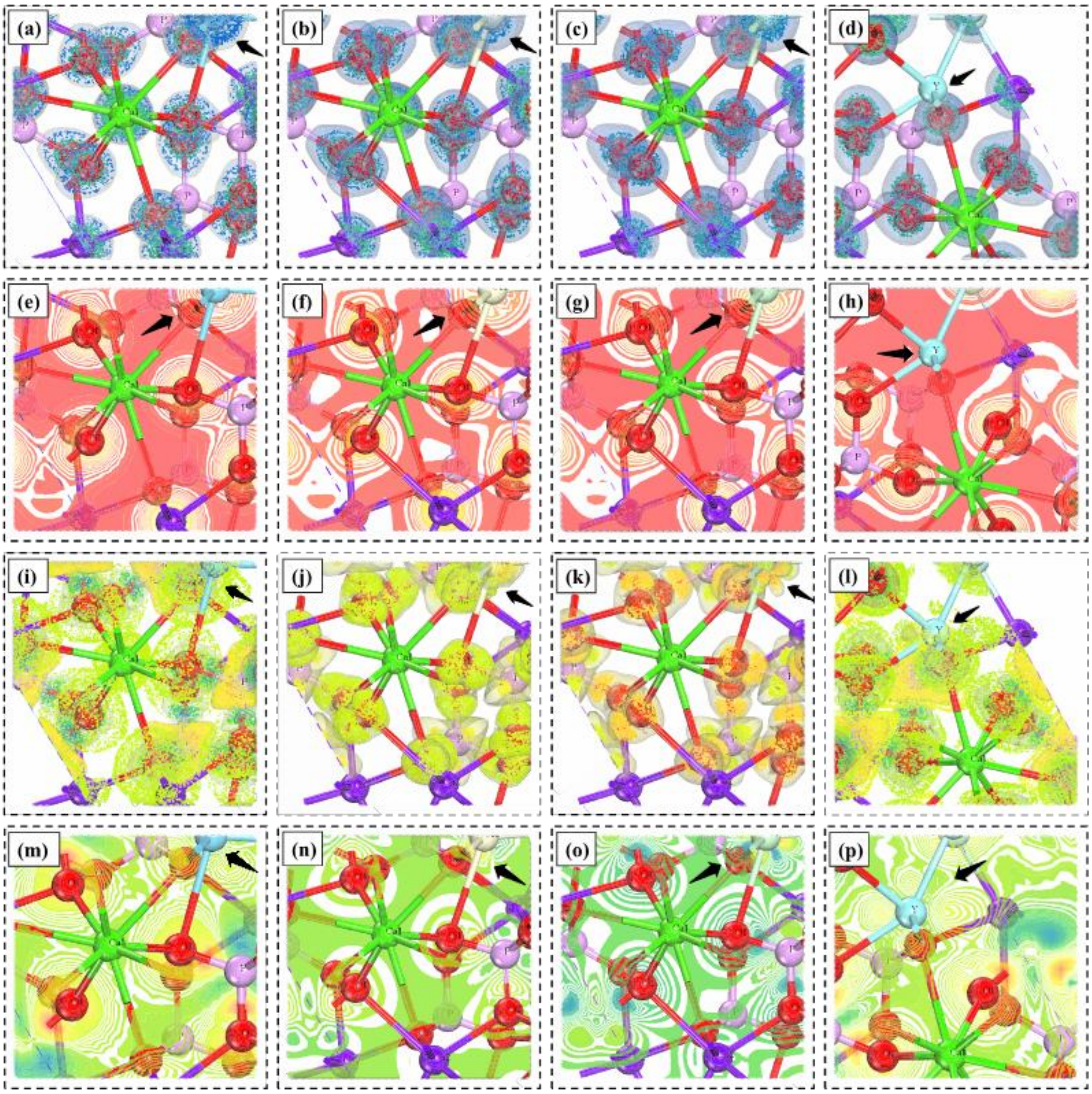

Fig. 9. Charge density and differential charge density of RE-doped FAP at the Ca1 site, where the black arrow points correspond to the charge density and differential charge density of La, Ce, Nd, and Y at the Ca1 site. (a-d) charge density isopotential of La, Ce, Nd, and Y at the Ca1 site, (e-h) the cross sections of the corresponding charge density isopotential, (i-l) differential charge density isopotential of La, Ce, Nd, and Y at the Ca1 site, (m-p) the cross sections of differential charge density isopotential surface of La, Ce, Nd, and Y at the Ca1 site.

4. Conclusions

The characterization results of synthetic products showed that La, Ce, Nd, and Y entered the FAP crystal, and one of every 20 Ca atoms in the crystal was replaced by one of La, Ce, Nd, and Y. The particle size of La, Ce, Nd, and Y-doped FAP was larger than that of FAP, because the secondary high-temperature process after adding RE promotes the secondary growth of the crystal. DFT+U calculation indicated that La, Ce, Nd, and Y can occupy the Ca1 (or Ca2) site theoretically and the substitution energy was negative. The substitution ability of La, Ce, and Nd at the Ca1 (or Ca2) site

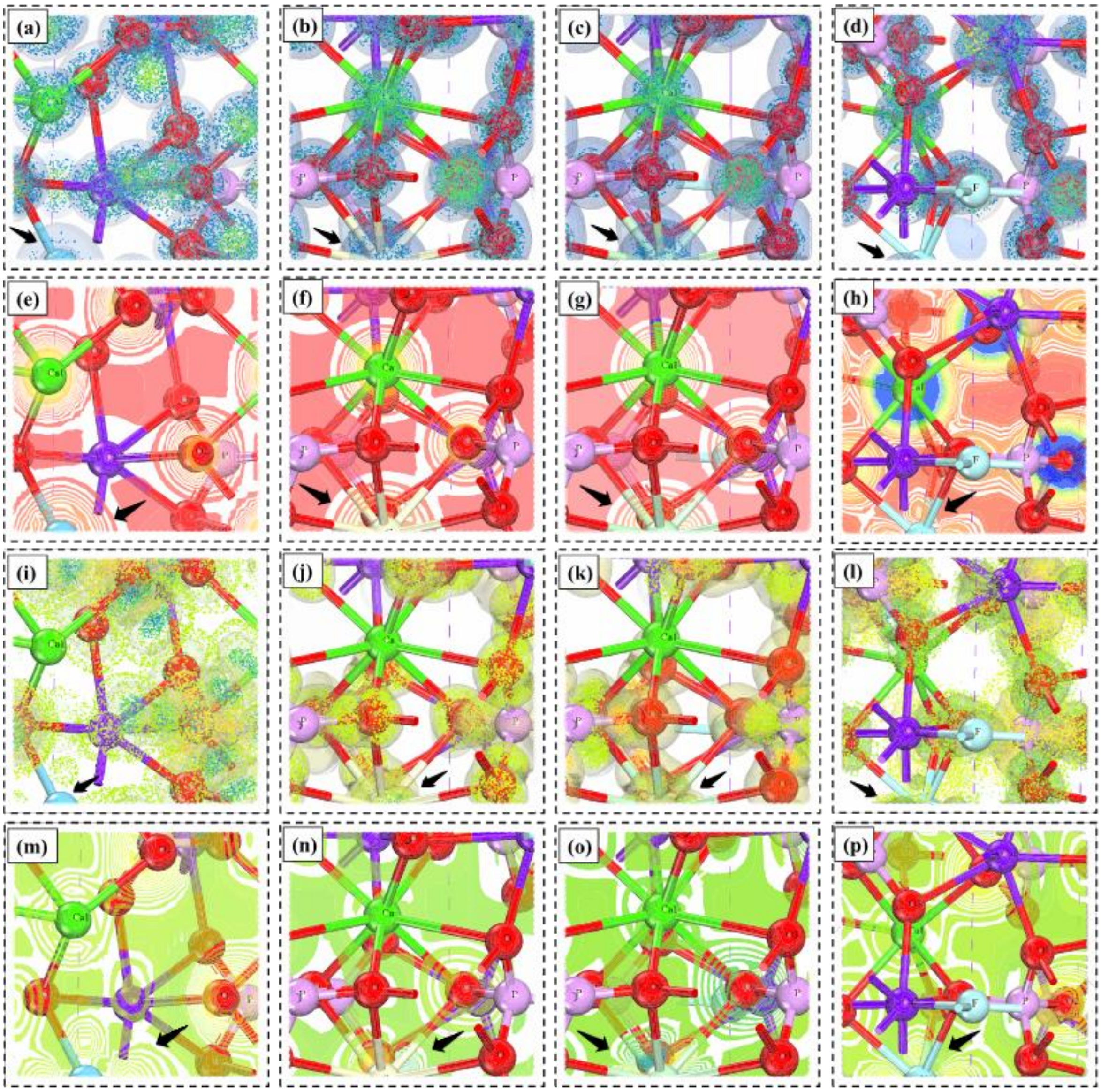

Fig. 10. Charge density and differential charge density of RE-doped FAP at the Ca2 site, where the black arrow points correspond to the charge density and differential charge density of La, Ce, Nd, and Y at the Ca2 site. (a-d) charge density isopotential of La, Ce, Nd, and Y at the Ca2 site, (e-h) the cross sections of the corresponding charge density isopotential, (i-l) differential charge density isopotential of La, Ce, Nd, and Y at the Ca2 site, (m-p) the cross sections of differential charge density isopotential surface of La, Ce, Nd, and Y at the Ca2 site.

increased gradually due to the contraction of lanthanide, and the radius was the main influencing factor. The substitution law of Y at the Ca1 (or Ca2) site did not show monotonic change compared with La, Ce, and Nd. The Y-O/F had both ionic and covalent bond components and the bonding strength was the strongest, which may be due to the role of spatial regulation in the crystal field. Mulliken bond populations of La-O/F, Ce-O/F, Nd-O/F, and Y-O/F contained both ionic bond and covalent bond components and range from 0.03 to 0.27. The covalency of RE-O and RE-F was enhanced compared with Ca-O and Ca-F after RE substitution. REs atom with unsaturated bond exposed on the surface of RE-bearing FAP will interact with the fatty acid collectors much more intensely compared to the FAP, which indicated that the existence of REs substitution may be in favour of the fluorapatite flotation. Differential charge density at the Ca2 site was greater compared with the Ca1 site and the corresponding bonding strength was greater. La, Ce, Nd, and Y tended to occupy the Ca2 site. The substitution difference of La, Ce, Nd, and Y at the Ca site of FAP was mainly caused by electron gain and loss of f and d orbitals. This study illustrated the doping law of RE in FAP, which provided a theoretical reference for the recovery of RE from phosphorite.

Acknowledgments

This work has been supported by the Talent Introduction Fund of Anhui University of science and technology (No. 132100025).

References

ABOUZEID, A.Z.M., NEGM, A.T., ELGILLANI, D.A., 2009. U*pgrading of calcareous phosphate ores by flotation: Effect of ore characteristics.* Int. J. Miner. Process. 90, 81–89.

ANISIMOV, V.I., ZAANEN, J., ANDERSEN, O.K., 1991. *Band theory and Mott insulators: Hubbard U instead of Stoner* I. Phys. Rev. B 44, 943–954.

BATAPOLA, N.M., DUSHYANTHA, N.P., PREMASIRI, H.M.R., ABEYSINGHE, A.M.K.B., ROHITHA, L.P.S., RATNAYAKE, N.P., DISSANAYAKE, D.M.D.O.K., ILANKOON, I.M.S.K., DHARMARATNE, P.G.R., 2020. *A comparison of global rare earth element (REE) resources and their mineralogy with REE prospects in Sri Lanka*. J. Asian Earth Sci. 200, 104475.

BOYER, L., SAVARIAULT, J.M., CARPENA, J., LACOUT, J.L., 1998. *A neodymium-substituted britholite compound.* Acta Crystallogr. Sect. C Cryst. Struct. Commun. 54, 1057–1059.

CHEN, J., YANG, R., WEI, H., GAO, J., 2013. *Rare earth element geochemistry of Cambrian phosphorites from the Yangtze Region*. J. Rare Earths 31, 101–112.

CLARK, S.J., SEGALL, M.D., PICKARD, C.J., HASNIP, P.J., PROBERT, M.I.J., REFSON, K., PAYNE, M.C., 2005. First principles methods using CASTEP. *Zeitschrift für Krist.* - Cryst. Mater. 220, 567–570.

COMODI, P., LIU, Y., ZANAZZI, P.F., MONTAGNOLI, M., 2001. *Structural and vibrational behaviour of fluorapatite with pressure. Part I: In situ single-crystal X-ray diffraction investigation*. Phys. Chem. Miner. 28, 219–224.

DUSHYANTHA, N., BATAPOLA, N., ILANKOON, I.M.S.K., ROHITHA, S., PREMASIRI, R., ABEYSINGHE, B., RATNAYAKE, N., DISSANAYAKE, K., 2020. T*he story of rare earth elements (REEs): Occurrences, global distribution, genesis, geology, mineralogy and global production*. Ore Geol. Rev.

EMERY, A.A., WOLVERTON, C., 2017. *High-Throughput DFT calculations of formation energy, stability and oxygen vacancy formation energy of ABO 3 perovskites*. Sci. Data 4, 1–10.

FILIPPOV, L.O., FILIPPOVA, I. V., KABA, O.B., FORNASIERO, D., 2021. *In-situ study of the kinetics of phosphoric acid interaction with calcite and fluorapatite by Raman spectroscopy and flotation*. Miner. Eng. 162, 106729.

FLEET, M.E., LIU, X., PAN, Y., 2000. *Site preference of rare earth elements in hydroxyapatite [Ca10(PO4)6(OH)2]*. J. Solid State Chem. 149, 391–398.

FLEET, M.E., PAN, Y., 1997. *Site preference of rare earth elements in fluorapatite; binary (LREE+HREE)-substituted crystals*. Am. Mineral. 82, 870–877.

FLEET, M.E., PAN, Y., 1995a. *Site preference of rare earth elements in fluorapatite. Am. Mineral.* 80, 329–335.

FLEET, M.E., PAN, Y., 1995b. *Crystal chemistry of Rare Earth Elements in fluorapatite and some calc-silicates.* Eur. J. Mineral. 7, 591–606.

FLEET, M.E., PAN, Y., 1994. *Site Preference of Nd in Fluorapatite [Ca10(PO4)6F2].* J. Solid State Chem. 112, 78–81.

HIMMETOGLU, B., FLORIS, A., DE GIRONCOLI, S., COCOCCIONI, M., 2014. *Hubbard-corrected DFT energy functionals: The LDA+U description of correlated systems*. Int. J. Quantum Chem. 114, 14–49.

HUANG, W., LIU, W., ZHONG, W., CHI, X., RAO, F., 2021. *Effects of common ions on the flotation of fluorapatite and dolomite with oleate collector*. Miner. Eng. 174, 107213.

HUGHES, J.M., CAMERON, M., MARIANO, A.N., 1991. *Rare-earth-element ordering and structural variations in natural rare-earth-bearing apatites.* Am. Mineral. 76, 1165–1173.

JAIN, A., HAUTIER, G., ONG, S.P., MOORE, C.J., FISCHER, C.C., PERSSON, K.A., CEDER, G., 2011. *Formation enthalpies by mixing GGA and GGA + U calculations.* Phys. Rev. B - Condens. Matter Mater. Phys. 84, 1–10.

JI, B., ZHANG, W., 2021. *Rare earth elements (REEs) recovery and porous silica preparation from kaolinite.* Powder Technol. 391, 522–531.

JIN, H.-X., WU, F.-Z., MAO, X.-H., WANG, M.-L., XIE, H.-Y., 2017. *Leaching isomorphism rare earths from phosphorite ore by sulfuric acid and phosphoric acid.* Rare Met. 36, 840–850.

LIU, H., LIAO, L., MOLOKEEV, M.S., GUO, Q., ZHANG, Y., MEI, L., 2016. *A novel single-phase white light emitting phosphor Ca9La(PO4)5(SiO4)F2:Dy3+: Synthesis, crystal structure and luminescence properties*. RSC Adv. 6, 24577–24583.

MILOJKOV, D. V., SILVESTRE, O.F., STANIĆ, V.D., JANJIĆ, G. V., MUTAVDŽIĆ, D.R., MILANOVIĆ, M., NIEDER, J.B., 2020. *Fabrication and characterization of luminescent Pr3+ doped fluorapatite nanocrystals as bioimaging contrast agents*. J. Lumin. 217, 116757.

MONKHORST, H.J., PACK, J.D., 1976. *Special points for Brillouin-zone integrations. Phys. Rev. B 13, 5188–5192.*

MULLIKEN, R.S., 1955a. Electronic population analysis on LCAO-MO molecular wave functions. I. J. Chem. Phys. 23, 1833–1840.

MULLIKEN, R.S., 1955b. *Electronic population analysis on LCAO-MO molecular wave functions. II. Overlap populations, bond orders, and covalent bond energies*. J. Chem. Phys. 23, 1841–1846.

NJEMA, H., BOUGHZALA, K., BOUGHZALA, H., BOUZOUITA, K., 2013. *Structural analysis by Rietveld refinement of calcium and lanthanum phosphosilicate apatites*. J. Rare Earths 31, 897–904.

PAN, Y., FLEET, M.E., 2002. *Compositions of the Apatite-Group Minerals: Substitution Mechanisms and Controlling Factors.* Rev. Mineral. Geochemistry 48, 13–49.

PAN, Y., FLEET, M.E., CHEN, N., WEIL, J.A., NILGES, M.J., 2002. *Site preference of Gd in synthetic fluorapatite by single-crystal W-band EPR and X-ray refinement of the structure: A comparative study.* Can. Mineral. 40, 3

PERDEW, J.P., BURKE, K., ERNZERHOF, M., 1996. *Generalized gradient approximation made simple*. Phys. Rev. Lett. 77, 3865–3868.

PERDEW, J.P., CHEVARY, J.A., VOSKO, S.H., JACKSON, K.A., PEDERSON, M.R., SINGH, D.J., FIOLHAIS, C., 1992. *Atoms, molecules, solids, and surfaces: Applications of the generalized gradient approximation for exchange and correlation*. Phys. Rev. B 46, 6671–6687.

PFROMMER, B.G., CÔTÉ, M., LOUIE, S.G., COHEN, M.L., 1997. *Relaxation of Crystals with the Quasi-Newton Method*, Journal of Computational Physics.

QIU, Y.Q., CUI, W.Y., LI, L.J., YE, J.J., WANG, J., ZHANG, Q., 2017. *Structural, electronic properties with different terminations for fluorapatite (0 0 1) surface: A first-principles investigation.* Comput. Mater. Sci. 126, 132–138.

ROUT, A., AGRAWAL, S., 2022. *Electronic and spectroscopic studies of rare earth doped yttrium strontium silicate fluorapatite compound*. Opt. Laser Technol. 152, 108108.

VANDERBILT, D., 1990. *Soft self-consistent pseudopotentials in a generalized eigenvalue formalism*. Phys. Rev. B 41, 7892–7895.

WANG, M., QIAN, R., BAO, M., GU, C., ZHU, P., 2018. *Raman, FT-IR and XRD study of bovine bone mineral and carbonated apatites with different carbonate levels*. Mater. Lett. 210, 203–206.

WANG, X., ZHANG, Q., MAO, S., CHENG, W., 2019. *A Theoretical Study on the Electronic Structure and Floatability of Rare Earth Elements (La, Ce, Nd and Y) Bearing Fluorapatite*. Minerals 9, 500.

XIE, J., LI, X., MAO, S., LI, L., KE, B., ZHANG, Q., 2018. *Effects of structure of fatty acid collectors on the adsorption of fluorapatite (0 0 1) surface: A first-principles calculations*. Appl. Surf. Sci. 444, 699–709.

XIE, J., ZHANG, Q., MAO, S., LI, X., SHEN, Z., LI, L., 2019. *Anisotropic crystal plane nature and wettability of fluorapatite.* Appl. Surf. Sci. 493, 294–307.

XIQIANG, L., HUI, Z., YONG, T., YUNLONG, L., 2020. *REE Geochemical Characteristic of Apatite: Implications for Ore Genesis of the Zhijin Phosphorite.* Minerals 10, 1012.

XUE, D., SUN, C., CHEN, X., 2017. *Hybridized valence electrons of 4f0–145d0–16s2: the chemical bonding nature of rare earth elements*. J. Rare Earths 35, 837–843.

ZHANG, Z., JIANG, Y., NIU, H., XING, J., YAN, S., LI, A., WENG, Q., ZHAO, X., 2021. *Enrichment of rare earth elements in the early Cambrian Zhijin phosphorite deposit, SW China: Evidence from francolite micro-petrography and geochemistry.* Ore Geol. Rev. 138, 104342.